Spaceborne imaging spectrometry of methane plumes: Quantifying the benefit of aerosol lidar

M. Queißer[1], S. Tomás[1], E. Armandillo[1], D. Vilaseca[1], D. Stepanova[1]

[1]AIRMO, Berlin, Germany

Corresponding author: Manuel Queißer manuel@airmo.io

Key Points:

- Aerosol extinction leads to biased methane enhancements (difference between plume and background XCH_4) if not accounted for by the retrieval
- The aerosol profile from lidar may constrain the retrieval, but it would miss the aerosol profile for the plume or the background
- Using end-to-end simulation in Monte Carlo mode suggests: A single profile from the swath center may still reduce the enhancement bias

Abstract (250 words max)

Column averaged mixing ratios of trace gases, such as methane (XCH_4), from spaceborne pushbroom spectrometers can be used to detect corresponding plumes and retrieve enhancements (ΔXCH_4), i.e., the difference between plume and background XCH_4. Over the global dust belt, however, significant scattering by dust aerosols may cause biased XCH_4 that may propagate into biased ΔXCH_4. To correct this, a co-aligned lidar could measure the aerosol profile in the middle of the scene (~20 km across track by 6 km along track). However, the vertical aerosol distribution may vary between the plume, covering hundreds of meters, and the background. Due to signal-to-noise requirements, only a single lidar profile per scene could be acquired, so either the plume or the background aerosol layer would be missed. Aerosol-induced bias would not be corrected equally for plume and background. A single lidar sounding in the center of the swath may, therefore, not improve the ΔXCH_4 bias. To test this hypothesis, end-to-end simulations in Monte Carlo mode were performed, simulating 2000 retrievals for randomized aerosol profiles and observation conditions. The use of a scattering radiative transfer model (RTM) constrained with aerosol profile data from a lidar at the swath center led to a reduced mean absolute bias of ΔXCH_4 (~0.5 ppb vs. ~2.6 ppb for an unconstrained RTM), with highest improvements for low albedo and strong plume/background albedo contrasts. This suggests that a pushbroom-lidar doublet could enable more accurate mass fluxes from point gas emitters, such as man-made greenhouse gas sources or volcanoes.

Plain Language Summary

To obtain methane enhancements (ΔXCH_4, plumes) and mass emission rates from imaging spectrometer retrievals, methane concentrations (XCH_4) at the plume and the background pixels are measured. Their difference yields ΔXCH_4. Soundings will be performed over atmospheres containing substantial amounts of dust aerosol, which modify light propagation. Both plume and background XCH_4 may thus be erroneous. This may cause erroneous ΔXCH_4 and mass flux estimates. To account for aerosol extinction, for the first time, a co-aligned micro-pulsed lidar, measuring the aerosol profile is proposed. But it could only deliver a single lidar profile for the entire scene (20 km across track by 6 km along track). The lidar would either miss the aerosol over the plume or the background. Therefore, XCH_4 could not be corrected equally for both and a ΔXCH_4 error is expected to remain, making the benefit of a lidar questionable. Assuming, a single aerosol type across the scene, smoothly transitioning between plume and background, we show by simulating many measurements under different observation conditions and aerosol distributions, that a single aerosol profile from lidar leads to fewer and lower ΔXCH_4 errors, especially for low albedo, high aerosol density and if albedo strongly varies between plume and background pixels.

1 Introduction

Over the last two decades, a new generation of satellites-borne imaging spectrometers with sub-kilometer pixel resolution emerged. This includes EnMAP (Guanter et al., 2015), EMIT (Thorpe et al., 2023), MethaneSAT (Dandenault et al., 2020) or CarbonMapper (Duren et al., 2025). These platforms can image and quantify atmospheric trace gas enhancements (plumes) over small areas, in particular, those from point emitters, such as CO_2 or CH_4 from oil and gas facilities. This enables direct quantification of fluxes of greenhouse gases (GHG) at a more regional or even local scale, contributing to improved emission inventories and emission factors.

Among these platforms are the first commercial EO missions such as GHGSat (Chan Miller et al., 2024), and AIRMO-Space. The latter has the aim to launch a satellite constellation of 12 MicroSat class spacecraft to detect and quantify methane plumes using pushbroom hyperspectral imaging in the short wave infrared (SWIR) region in target mode, providing the following data products: Level-2 (L2, images of CH_4 column averaged mixing ratios, XCH_4), Level-3 (L3, plume masks with CH_4 enhancements, ΔXCH_4) and level-4 (L4, mass emission rates or fluxes).

Following end-to-end simulations, the performance budget to reach the envisaged L4 sensitivity of 100 $kgCH_4h^{-1}$ from point emitters entails a target precision and bias of 16 $ppbCH_4$ and -0.5 to 3.3 $ppbCH_4$, respectively, comparable to missions with similar objectives (Noël et al., 2024; MacLean et al., 2025).

The in-orbit-demonstration (IOD) will concentrate on oil and gas operations in areas in North Africa, Middle East and Asia. Large extends of this region are located in the Dust Belt (Milford et al., 2019; Tindan et al., 2023), where an aerosol optical depth (AOD) >0.1 is expected at many locations all year around, based on AERONET data (Holben et al., 1998). Over these areas, light scattering and absorption by aerosols may significantly modify the path of downwelling and upwelling solar photons, leading to over- or underestimated trace gas column densities, i.e., biased XCH_4 (Butz et al. 2012; Somkuti et al. 2025).

Proxy gas retrieval using XCO_2 (Frankenberg et al.; 2005, 2025; Krings et al., 2011; Schepers et al., 2012; Staebell et al., 2021) is viable and considered for the current mission. However, for areas where homogeneous XCO_2 cannot be assumed, including urban areas (Klausner et al., 2020; Zhu et al., 2022), or near large geological CO_2 emitters (Di Martino et al., 2024), we deem a physics-based retrieval, i.e. modeling aerosol extinction during the L2 retrieval, the most adequate. This requires a scattering forward radiative transfer model (scattering RTM, SRTM), which in turn needs an aerosol parametrization, such as in the form of aerosol layer height (ALH), aerosol layer width (ALW) and AOD (Dubovik et al., 2011; Butz et al., 2012). ALH and ALW are commonly retrieved indirectly by measuring and inverting the Oxygen A-band absorption, which, however, may entail uncertainties of the order of ~1 km (Jänicke et al., 2023; Kim et al., 2024).

To achieve more direct and potentially more accurate measurements of the aerosol profile, a dedicated micro aerosol lidar, co-aligned with the imaging spectrometer, is planned to be part of the payload. Simulations for AOD >0.1 and a consequent lidar signal-to-noise ratio (SNR) ≥ 3 yielded range uncertainties <200 m. The pulsed lidar will probe the entire atmospheric column beneath the spectrometer, directly measuring the aerosol attenuated backscatter profile, and thus the vertical aerosol distribution (ALH, ALW and potentially AOD).

The latter would constrain the SRTM, which would effectively improve vertical sensitivity of the retrieval as quantified by the methane averaging kernel (AK), a diagnostic metric calculated as $AK = GK$, where G is the gain vector (for CH_4, in ppb per photons/s/m^2/sr/nm) and K the Jacobian matrix. The latter specifies the sensitivity of the forward modeled radiance to a change in a state vector element at a given vertical atmospheric layer of the RTM and thus the vertical retrieval sensitivity of the total column XCH_4. It describes how a perturbation of methane concentration in a given layer (relative to the prior) propagates into the retrieved total column XCH_4. Aerosol scattering would be allocated at the correct altitude, improving the Jacobian and thus the AK. A SRTM constrained with accurate ALH and ALW would therefore reduce misinterpretation in the L2 retrieval, particularly when aerosols are not vertically co-located with trace gas accumulations, as it would help to differentiate between a radiance perturbation due to aerosol or gas.

However, following lidar sensitivity analysis, to reach the minimum SNR, the lidar would be integrating pulses during tens of seconds, while a forward motion compensation (FMC) maneuver is executed from a zenith angle of about -15° to 15° (Fig. 1a). The corresponding scene length (along track) would be ~6 km and the scene width (across track) would be ~20 km.

Full 2D end-to-end (E2E) simulations using 100 $kgCH_4h^{-1}$ plumes from large eddy simulations (LES) suggest numerous scenarios where either the background or the plume would be outside the lidar field of view (FOV) of ~130 m (e.g., Fig. 1b). The lidar would basically perform a slice-scanning in the swath center and along the flight track, yielding an average measure of the aerosol profile along track. It would miss aerosol left and right of its FOV, i.e., over the background or plume pixels, whichever are not beneath the lidar. This leads to the main question of the paper: The potential benefit of aerosol profile from such a lidar sounding.

The latter is critically questioned in the following, leading to the hypothesis. In the method section, the simulation scheme used to test the hypothesis is detailed. In the result section, the simulation results are presented and discussed.

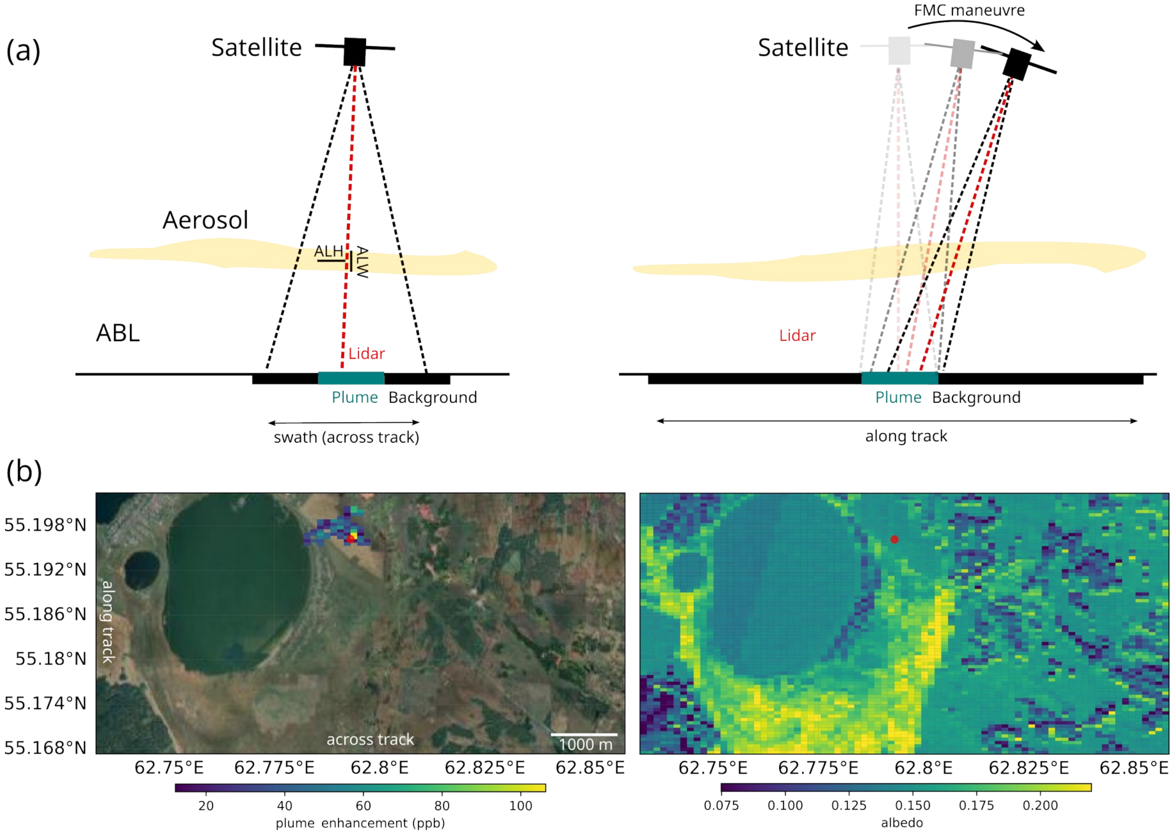

Figure 1. Observation situation. (a) Schematic view of measurement geometry with a staring lidar co-aligned with the push broom spectrometer. In this example the background XCH_4 is off the center swath, whilst the XCH4 enhancement (plume) is at the center of the swath. Left: across track view. ALH and ALW are measured in the swath center. Right: Along track view depicting the forward motion compensation (FMC). ALH and ALW represent average values over the probed track. ABL depicts the atmospheric boundary layer. Figure not to scale. (b) Simulated scene (zoom) with retrieved L3 enhancements from a LES plume for 100 $kgCH4h^{-1}$ flux and 2 ms^{-1} wind speed (simulation with enhancement form a LES plume) over satellite imagery (Source of background tiles: Google). Easting is aligned with across-track. The red dot depicts the randomly chosen source location. Right: Albedo from Sentinel-2 of the same location. Re-gridded to GSD of instrument (50 m along track and 100 m across track).

3 Material and Methods

3.1 Null hypothesis

The key quantity of interest for this mission is ΔXCH_4, i.e., the difference between plume and background XCH_4 (L3, enhancement). In an idealized model, assuming a plume and a background pixel with equal surface reflectivity, atmosphere and solar irradiance, respectively, the retrieved, aerosol-biased XCH$_4$ for plume and background could be written as

$$XCH_{4,pl,biased} = XCH_{4,pl} + G\left(y_{aero,pl} - y_{aero,lidar}\right),$$

and

$$XCH_{4,bg,biased} = XCH_{4,bg} + G\left(y_{aero,bg} - y_{aero,lidar}\right). \qquad (1)$$

Let G be the (spectrally dependent) gain vector and $y_{aero,pl}$ and $y_{aero,bg}$, the fraction of the radiance caused by aerosol scattering over plume and background, both unexplainable by the RTM, and $y_{aero,lidar}$ the radiance explained by a SRTM constrained with an aerosol profile from the swath center. $X_{CH4,pl}$ and $X_{CH4,bg}$ are the mixing ratios if no aerosol was present. In the retrieval used here, the enhancement (L3) would then be

$$\Delta XCH_4 = X_{CH4,pl,true} - X_{CH4,bg,true} + \varepsilon_{\Delta XCH4}, \qquad (2)$$

with the L3 error, i.e., the aerosol-induced enhancement bias,

$$\varepsilon_{\Delta XCH4} = G\left(y_{aero,pl} - y_{aero,bg}\right). \qquad (3)$$

$y_{aero,lidar}$ constrained by a single aerosol profile canceled in Eq. (2) and any existent bias, Eq. (3), remains, i.e., is not corrected. From Eq. (3) it also follows that if the aerosol induced bias of plume and background are equal, such as when the aerosol profile is the same for plume and background, the bias would cancel. The effect of a lidar would be nullified in both cases.

However, the above model oversimplifies reality, for instance, in assuming equal observation conditions, spectral gain for plume and background and linearity of the retrieval response. A single aerosol profile for the scene, such as retrieved from lidar, could still give a smaller enhancement bias compared to not correcting for aerosol scattering. To assess this, the following null hypothesis was tested: A single measured aerosol profile per scene does not reduce the ΔXCH$_4$ bias $\varepsilon_{\Delta XCH4}$.

3.2 Simulation approach

To test the null hypothesis, end-to-end simulations were performed using a Monte Carlo simulation (MCS) approach. A single aerosol layer was assumed, smoothly varying in height (ALH), width (ALW) and aerosol number density (parametrized as AOD), over the scene, including the enhancement (plume). MCS using full scenes with hundreds of across-track and along track pixels, respectively, would be computationally expensive. Moreover, it would add another layer of complexity in identifying statistical difference in L3 bias with/without SRTM. Therefore, the smallest possible scene was simulated: a “plume pixel”, containing the enhanced methane column, and a “background pixel”, which contains only the background methane column. Although a simplification, this two-pixel scene is deemed to conserve the essential radiative transfer physics that governs the biases in L2 and L3. The plume was assumed to be at the swath center, probed by the lidar, the background pixel was off the swath center and not probed by the lidar (as in Fig. 1b). This is arbitrary and reversing this assumption would not reduce generality.

Considering a L4 sensitivity requirement of ~100 kgCH$_4$h^{-1}, the true enhancement $\Delta XCH_{4,true}$ was estimated using a simple slab mass balance model (Gerilowski et al., 2011), linking methane enhancement and plume transport speed to mass emission rate (flux). The column enhancement was assumed to be equally spread over a plume width of 160 m. Assuming a wind speed of 1 ms^{-1} entails a column enhancement of ~6.5×10^{21} molec.m^{-2} or ~1.6%, assuming a background XCH$_4$ of 1900 ppb. This corresponds to a ~30 ppb enhancement adding to an assumed 1900 ppb background methane mixing ratio.

A complete MCS run consisted of the following steps:

1. Simulate top-of-atmosphere (TOA) radiance for the plume pixel with plume aerosol profile, XCH$_4$ 1930 ppb
2. Simulate TOA radiance for the background pixel with background aerosol profile, XCH$_4$ 1900 ppb
3. Retrieve XCH$_4$ (L2) for plume pixel using the SRTM
4. Retrieve XCH$_4$ for background pixel using the SRTM
5. Retrieve XCH$_4$ for plume pixel using the NSRTM
6. Retrieve XCH$_4$ for background pixel using the NSRTM
7. Compute ΔXCH$_{4,\,SRTM}$ and ΔXCH$_{4,NSRTM}$
8. For both, compute the L3 bias as

$$\varepsilon_{\Delta XCH4} = \Delta XCH_4 - \Delta XCH_{4,true} = \left(XCH_{4,pl} - XCH_{4,pl,true}\right) - \left(XCH_{4,bg} - XCH_{4,bg,true}\right) \quad (4)$$

Equation (4) shows that the L3 bias is the difference between the L2 bias of plume and background.

The steps outline above were executed for 2000 random measurements (random draws), of observation conditions (OC, albedo and solar and viewing azimuth and zenith angles) and aerosol profiles, parameterized by ALH, ALW, AOD. Henceforth, a “measurement” refers to one of the 2000 retrievals.

As an accuracy metric, which assesses the statistical significance of using a constrained SRTM over a NSRTM, the mean absolute error (MAE) of the enhancement was computed as

$$MAE = \frac{1}{2000}\sum_{i=1}^{2000}\left|\varepsilon_{\Delta XCH4}\right|_i \quad (5)$$

3.3 End-to-End simulator overview

In the following, the end-to-end simulator (E2E) used to simulate TOA radiance and retrieve XCH$_4$ for the push broom spectrometer is briefly described (Fig. 2a). Table 1 summarizes the key parameters used. Text 1 in the supporting information gives more details on the NSRTM, SRTM, L2 retrieval and aerosol parametrization.

Given a set of OC and aerosol profile (AOD, ALH, ALW), for a given pixel, the scene generation module (SGM) calculates a TOA spectra using the SRTM, accounting for absorption of H_2O, CO_2 and CH_4 (Table 1) and assuming transported mineral dust aerosol across the whole scene (Sugimoto et al., 2020; Ratcliffe et al., 2024). This aerosol type was deemed representative for the mission's region of interest. True ALH, ALW and AOD (Table 1) are representative values adopted from the AERONET observational network (Holben et al., 1998). The aerosol type specific single scattering albedo and scattering phase function (Fig. S3 in the supporting information) were taken from the OPAC catalogue (Hess et al., 1998).

Table 1. Push broom and E2E simulation parameters and aerosol scenario used for all simulations with default AOD, ALH and ALW.

Parameter type	Value
Spectral range for SGM and L2	1590 nm - 1670 nm
Spectral resolution (ISRF)	0.9 nm (FWHM)
Ground pixel size	50 m along tracking 100 m across track
Swath width	20 km
Sensor altitude	500 km
True XCH_4 background	1900 ppb
True XCH_4 plume	1930 ppb
True XCO_2 (plume and background)	425 ppm
P, T, spec. humidity	US-Standard Atmosphere
Aerosol type	Transported mineral dust
AOD	0.21
ALH	2500 m
ALW	750 m
Single scattering albedo @ 1550 nm	0.925
Mie scattering 4π phase function at 150° scattering angle	0.248

Since the SNR of the lidar is relatively low, AOD was assumed not retrievable from the lidar signal, but instead was assumed to be known reasonably well from observational networks, such as AERONET. This was mimicked by setting the retrieval AOD used in the L2 forward modeling to the mean AOD between plume and background pixel for all MCS runs. A corresponding sensitivity test assessing the effect of the AOD knowledge error is provided in the supporting information, text S2.

To simulate a realistic, smoothly varying true aerosol layer between plume and background (Fig. 1), the parameters of the background aerosol layer (i.e., ALW, ALH, AOD) were drawn from a random distribution (mean/STD: 2500 m/700 m, 750 m/400 m, 0.21/0.13).

Smoothly correlated ALW, ALH and AOD for the plume pixel were simulated by perturbing the background aerosol parameters by a random number with mean 1 and STD of 0.1 (10%). Figure S2 (supporting information) shows example distributions for all parameters. Figure 2b shows an example aerosol profile as used in the SGM.

To avoid correlation, mimicking random differences in plume/background albedo (e.g., forest/crop/rock/urban boundaries, Fig. 1b), the plume and background albedo values were drawn from two different random distributions. Viewing zenith angles (VZA) were different for plume and background, but drawn from the same random distribution, i.e., not independent. While random, solar zenith/azimuth (SZA, SAA) and viewing azimuth angles (VAA) were the same for plume and background. ALH and ALW were clipped to a minimum of 300 and 200 m, respectively. AOD was clipped to an interval of [0.02, 1], VZA, VAA, SZA, SAA were clipped to [0°,20°], [0°,360°], [0°,70°], [0°, 360°], respectively. Albedo values were clipped to [0.1, 0.8].

The L0 radiance for each pixel is input to an instrument model (Fig. 2a), which simulates the measurement process. In the configuration used here, to isolate the effect of aerosol scattering, no instrument noise and no instrument errors were simulated. Only the degradation in spectral resolution was simulated by convolving the TOA radiance with a Gaussian instrumental spectral response function (ISRF), leading to simulated raw spectra (Level-0, L0) for each pixel. These are passed to the L0-L1b module, which converts them to instrument corrected and calibrated radiance spectra (L1b, Fig. 2a).

In the L2 processor, the L1b spectrum is fitted to a forward modeled radiance spectrum, using either the SRTM or the NSRTM, resulting in column averaged mixing ratios XCH_4 (Fig. 2a). Both the L1b-L2 and the SGM module use the same SRTM.

3.4 Lidar simulation

The sole aim of the lidar simulation was to obtain a realistic noise (uncertainty) estimate for lidar-retrieved ALH and ALW. Design parameters, such as repetition rate, optical power, aperture, receiver bandwidth as well as the lidar simulator itself are out of scope and will be detailed in a separate article. We assume here that the lidar can yield $SNR \geq 3$. The lidar simulation evaluates the attenuated backscatter (Fig. 2c), which results from the same aerosol profile as for SGM (e.g., Fig. 2b, but fixed AOD 0.21, ALH 3 km and ALW 750 m) and the lidar ratio. This is followed by a detector module.

Noise was calculated as the contributions of signal, solar background and dark counts of shot noise. The TOA radiance from the E2E SGM module was used to simulate solar background photon noise as part of the SNR calculation for the lidar signal. The SNR was determined by the desired range resolution and the measurement time for signal and background. The noise was added to the expected signal based on the SNR profile. The resulting SNR was 4.

ALH and ALW were retrieved by fitting a Gaussian curve to the noisy lidar signal, Fig. 2d. To assess uncertainty (mean and standard deviation, STD) of ALH and ALW, this procedure was repeated in Monte Carlo manner with 1000 realizations of random noise, all associated with SNR 4. This yielded ALH 3.09 ± 0.126 km and ALW 0.736 ± 0.144 km (uncertainties are sample STD). The corresponding relative errors were adopted as representative lidar measurement uncertainties of ALH and ALW during L2 retrieval by multiplying them with the true ALH and ALW for the plume (swath center).

For simplicity, the lidar SNR was fixed for all 2000 end-to-end retrievals. Lidar OC were fixed (albedo 0.3, VZA 0°, SZA 30°), but close to the median of those OC of the MCS, whilst the SZA is relatively low. This makes the solar background noise, the most dominant noise source, a conservative estimate.

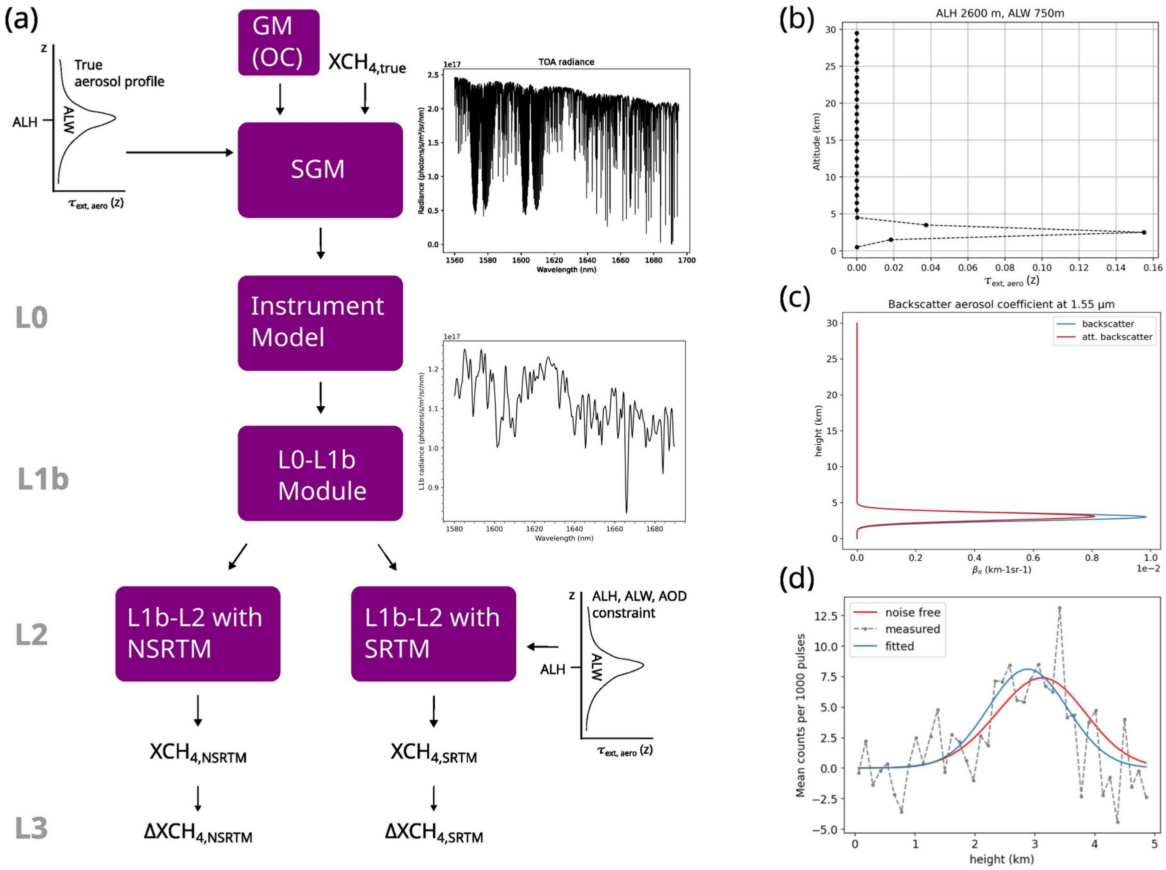

Figure 2. (a) End-to-end simulation scheme (E2E) for a given pixel with geometry module (GM/OC), scene generation module (SGM), instrument module, L0-L1b module, and L1b-L2 module which includes the forward model. Example TOA and L1b spectra are shown. (b) Example discretized AOD profile as used in E2E. (c) Backscatter and attenuated backscatter profile input for lidar simulation. (d) Simulated range corrected lidar signal resulting from (c) with and without noise (SNR 4) and Gaussian fit.

4 Results

4.1 Single central lidar with noise

For the first scenario, a single aerosol profile constrained by lidar soundings was assumed. Table 2 shows the first 10 out of 2000 MCS results. Figure 3 shows the histograms of L2 and L3 results and L3 errors for the SRTM and NSRTM case. Also shown is the cumulative probability distribution of the absolute L3 errors for both models.

Not accounting for aerosol scattering in the RTM (using a NSRTM) leads to a negatively biased XCH_4 for all measurements (underestimated truth, Fig. 3a). Depending on the scenario (OC, aerosol profile), minimum L2 biases were -76 $ppbCH_4$ (-64 $ppbCH_4$) for plume (background) pixels (Fig. 3a). The mean absolute L3 bias magnitude is 2.56 $ppbCH_4$ (MAE, Fig. 3b). There are L3 bias magnitudes larger than that, associated with L2 bias below -10 $ppbCH_4$ (e.g., rows 2, 4, Table 2) where albedo was low (< 0.2) for plume and/or background. The corresponding mechanisms will be detailed in the discussions.

For the lidar-constrained SRTM, the shift of the cumulative probability distribution (Fig. 3b) towards lower values, and the MAE of 0.49 $ppbCH_4$, indicates a substantial improvement of L3 bias averaged over the 2000 measurements. This is due to L2 biases being smaller than for the NSRTM and, due to lower unexplained residual radiance, more equal for plume and background, especially for measurements with higher plume/background albedo contrast (e.g., rows 2, 5, 6 in Table 2). As further detailed in the discussion, the XCH_4 biases for the background are larger than for the plume, but still lower than for the NSRTM (spread of histogram, Fig. 3a).

Table 2. First 10 out of 2000 MCS results for the single central lidar with noise scenario. ret depicts retrieval, pl and bg stand for plume and background, respectively.

ALH pl (m)	ALW pl (m)	AOD pl	ALH bg (m)	ALW bg (m)	AOD bg	ALH ret (m)	ALW ret (m)	Albedo pl	Albedo bg	SZA (°)	VZA pl (°)	VZA bg	VAA (°)	SAA (°)	XCH4 pl SRTM (ppb)	XCH4 bg SRTM (ppb)	XCH4 pl NSRTM (ppb)	XCH4 bg NSRTM (ppb)	$\varepsilon_{\Delta XCH4}$ SRTM	$\varepsilon_{\Delta XCH4}$ NSRTM
2208	1166	0.2	1950	1030	0.21	2211	1018	0.33	0.26	57	5	7	115	89	1929.85	1900.09	1927.47	1897.01	-0.24	0.46
2461	1342	0.29	2630	1440	0.3	2559	1351	0.14	0.44	51	17	20	138	185	1930.36	1899.66	1918.51	1895.74	0.7	-7.23
1005	832	0.18	780	640	0.19	956	1122	0.49	0.5	22	18	20	157	93	1929.9	1900.12	1928.8	1899.06	-0.22	-0.26
3648	875	0.42	4320	1040	0.39	3711	819	0.31	0.17	56	5	6	152	205	1929.75	1897.72	1918.54	1879.56	2.03	8.97
1245	1126	0.35	1180	1070	0.31	1242	846	0.27	0.1	24	10	13	23	166	1929.46	1900.07	1926.47	1893.46	-0.6	3.01
1911	820	0.27	1650	710	0.29	2044	1116	0.2	0.38	40	9	12	224	183	1930.36	1900.42	1924.69	1897.01	-0.06	-2.31
2852	993	0.3	2630	910	0.29	2851	972	0.47	0.32	35	6	7	110	126	1929.75	1900.29	1925.74	1894.5	-0.53	1.24
1628	832	0.32	1960	1000	0.35	1664	857	0.19	0.21	1	17	20	198	141	1930.3	1898.19	1921.43	1890.39	2.11	1.05
1759	758	0.02	2130	920	0.02	1731	898	0.43	0.54	19	7	9	55	131	1929.8	1899.77	1929.63	1899.64	0.02	-0.01
1864	494	0.02	1840	490	0.02	1970	481	0.26	0.41	47	6	8	81	128	1929.82	1899.82	1929.65	1899.71	0.00	-0.06

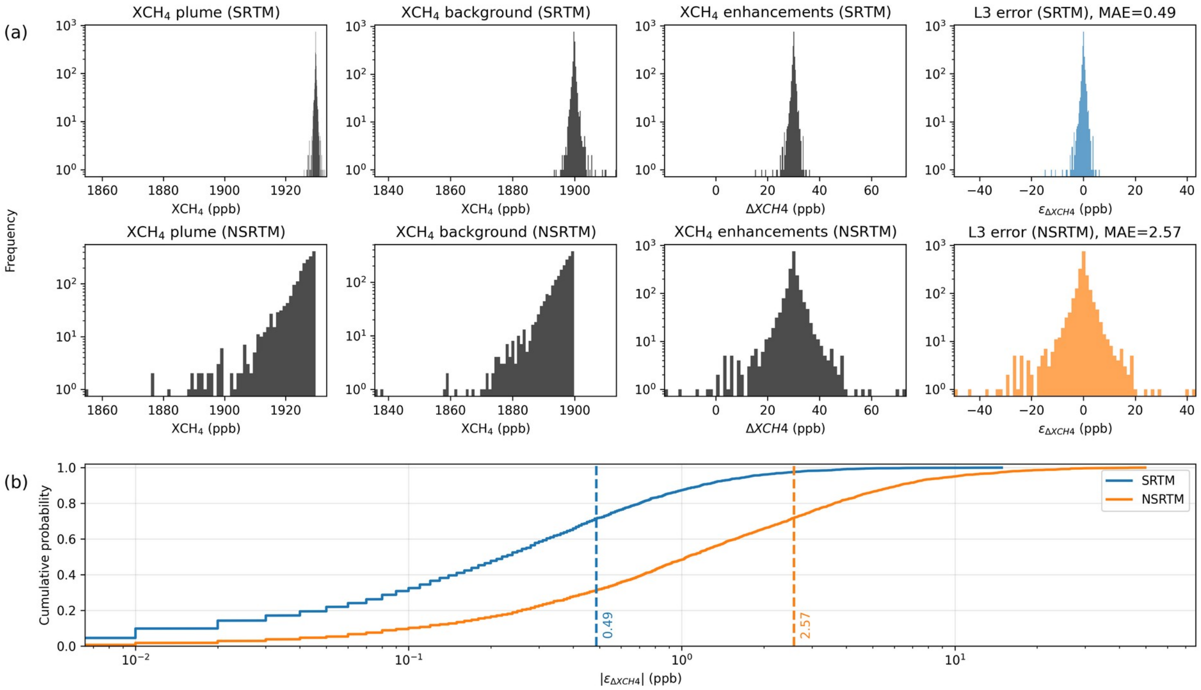

Figure 3. Results for the single central lidar with noise scenario. (a) Histograms of plume and background L2 results, L3 results and L3 bias for the SRTM and NSRTM case. (b) Empirical cumulative distribution of absolute L3 errors for SRTM and NSRTM with MAE depicted.

4.2 Fixed guess single central aerosol profile

For the second scenario, the true aerosol profiles were equal to the previous scenario. However, no lidar aerosol profile measurements were used to constrain the SRTM. Instead, the retrieval ALH and ALW were fixed to 2000 m and 800 m, respectively, for all 2000 measurements. For many of the 2000 measurements, the fixed guess aerosol profile was reasonably close to the true aerosol profile. For example, for almost half of the measurements, ALH was within 500 m of the truth. Hence, a L3 bias improvement below but comparable to the lidar scenario was achieved (MAE 0.82 ppbCH$_4$). This suggests that a SRTM constrained by a constant guess ALH and ALW, not necessarily from lidar, can be beneficial. Aerosol profile data could be obtained from external sources, such as EarthCare (Wandinger et al., 2023), TROPOMI (Sun et al., 2019) or the MODIS instrument (Lyapustin et al., 2011). Whether this could be done in near real time and close to the sounding area requires further investigation. Entirely relying on third party data sources could risk data availability, which would make a lidar preferable. Third sources could still be consulted to validate lidar data or to complement it, if lidar soundings fail.

4.3 Random guess aerosol profile

This MCS scenario was identical to the fixed guess run, except that for each measurement the SRTM was constrained with a random guess aerosol profile with mean/STD of 4000 m/3000 m for ALH and 1000 m/700 m for ALW.

The resulting MAE of 2.1 ppbCH_4 is comparable to ignoring aerosol extinction (NSRTM case). The L2 bias distributions are equally broad for SRTM and NSRTM (Fig. 4a) and cumulative probabilities are only slightly distinct (Fig. 4b). The overlapping tails indicate that frequency and magnitude of large L3 bias is not reduced. This suggests that a randomly constrained SRTM would not be beneficial for aerosol correction.

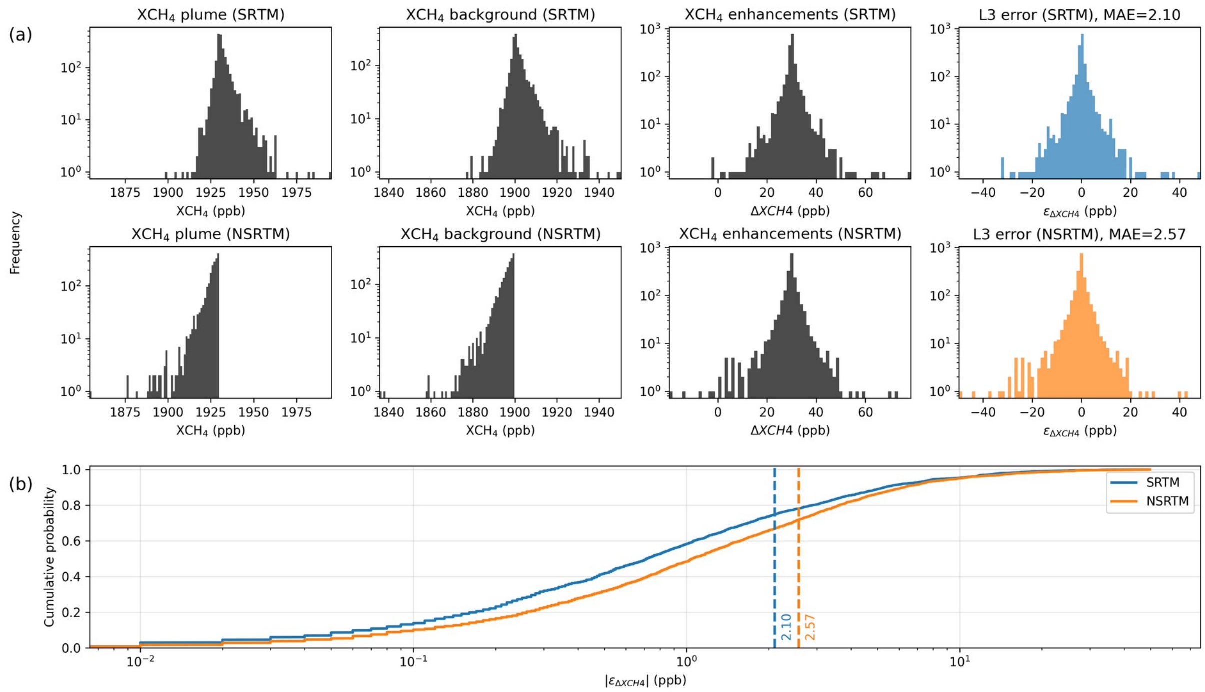

Figure 4. Results for the random guess scenario. (a) Histograms of plume and background L2 results, L3 results and L3 bias for the SRTM and NSRTM case. (b) Cumulative distribution of absolute L3 errors for SRTM and NSRTM with MAE depicted.

5 Discussion

5.1 Level-3 bias and implications for methane fluxes (Level-4)

The MAE quantifies the absolute mean spread of the L3 (ΔXCH_4) bias values, $\left|\varepsilon_{\Delta XCH4}\right|$. For the single central lidar scenario, for both the NSRTM and SRTM, $\varepsilon_{\Delta XCH4}$ are fairly normal distributed with a mean close to zero for both NSRTM (-0.27 ppbCH_4) and SRTM (-0.02 ppbCH_4). The SRTM, if sufficiently constrained, thus reduces the magnitude of the L3 bias on average, but it does not cause a notable systematic shift in ΔXCH_4.

The transported mineral dust aerosol scenario entailed a MAE of ~2.6 ppbCH_4, when ignoring aerosol extinction in the retrieval (NSRTM in Table 3). L3 bias ranged from -49.8 ppbCH_4 to 43.3 ppbCH_4 (Fig. 3a). The SRTM constrained by a single aerosol profile from only the plume, but not the background, partly corrects for scattering at both plume and background. It increases accuracy of both plume and background forward modeled radiance, and consequently reduces XCH_4 bias for both. This leads to a reduced L3 bias magnitude (Eq. (4)) on average, i.e., a reduced MAE. With lidar, or a close guess, the MAE was reduced to 0.49 ppbCH_4 and 0.83 ppbCH_4, respectively (scenarios 1 and 2, Table 3).

What would be the L4 (flux) error when ignoring aerosol scattering? Assuming a constant column averaged ΔXCH_4 of 30 ppbCH_4 across the plume, the MAE of 2.6 ppbCH_4 corresponds to an average relative L3 error of ±8.5%. Adopting the aforementioned plume model (160 m wide plume, 1 ms^{-1} wind speed, ~100 $kgCH_4h^{-1}$), to first order, the propagated average bias would be roughly ±9 $kgCH_4h^{-1}$. MCS were repeated for column enhancements of 20, 10 and 5 ppbCH_4. The bias remained approximately constant. This suggests that for lower CH_4 fluxes, the average relative L3 (and L4) error would be higher, e.g., ~27% for a ΔXCH_4 of 10 ppb, provided enough sensitivity to resolve this enhancement.

Even if aerosol scattering is constrained, there are few cases with considerable L3 bias (Fig. 3b). However, these cases are significantly reduced in magnitude and occurrence compared to an unconstrained SRTM or a NSRTM. This is reflected in the tails of the L3 error distribution. In the lidar constrained SRTM scenario (Fig. 3b), for only 47 cases (~2%) the L3 bias magnitude was >2.6 ppbCH_4. For 8 measurements (0.4% of all measurements), the L3 bias magnitude was ≥5 ppbCH_4, the highest corresponding to -14.85 ppbCH_4. These are cases with a large difference between retrieval ALH and background ALH, which the lidar does not measure. The underlying mechanisms will be detailed further below.

For those cases, however, the NSRTM L3 bias was even higher. For the NSRTM, 556 measurements (~28%) entail a L3 error magnitude >2.6 ppbCH_4. In 270 cases (~13.5% of measurements) the L3 bias magnitude was ≥5 ppbCH_4, with extreme values of -49.8 ppbCH_4/43.3 ppbCH_4 (min/max), that is, higher than the 30 ppbCH_4 enhancement. Therefore, in 13.5% of the cases, L3 bias would be ~17% to >100%, with corresponding first order L4 errors.

The L3 biases of this study are in line with those found by Yu et al. (2024), who simulated enhancement methane bias near 1666 nm for different aerosol types near industrial sites and with the lower end L3 biases found by Huang et al. (2020), who simulated L3 bias near 2 µm for an airborne sensor altitude using an aerosol mixture.

Table 3. Summary of all MAE for all simulated scenarios.

Nr.	**Scenario**	**MAE ($ppbCH_4$) (SRTM)**	**MAE ($ppbCH_4$) (NSRTM)**
1	Single central lidar with noise	0.49	2.57
2	Constant guess aerosol profile	0.83	2.57
3	Random guess aerosol profile	2.10	2.57
4	Single central lidar with noise, aerosol near ground	0.25	1.29
5	Ideally constrained, different aerosol profile, equal OC	0.003	0.69
6	Ideally constrained, constant aerosol profile, equal OC	0.002	0.09
7	Ideally constrained, constant aerosol profile, different OC	0.003	2.50

5.2 Level 2 bias

The observed mean L2 error over all 2000 runs, when not accounting for aerosol scattering (NSRTM), is -5 $ppbCH_4$ (-4.7 $ppbCH_4$) for the plume (background), or about -0.26%, and thus compatible to Butz et al. (2012), who simulated aerosol induced L2 bias in the 2 µm spectral region.

5.2.1 Bias mechanisms for the NSRTM L2 bias

The negative bias as a result of ignoring aerosol extinction in L2 retrieval can be explained by a path shortening effect, which is pronounced when the aerosol layer is located above the methane accumulation in the lower atmospheric boundary layer. This reduces the sensitivity of the simulated TOA radiance to the near-surface, methane-rich atmospheric layers. The apparent depth of the molecular absorption lines is smaller, similar to a dimming effect, since less photons traverse the near-surface layers. Once albedo cannot be optimized further, the NSRTM retrieval lowers the trace gas vertical column density (VCD), resulting in a systematic underestimation of absorption and thus total column XCH_4. This is also reflected in the anti-correlation between XCH_4 and AOD and the weak anti-correlation of XCH_4 with ALH (Fig. 5): The higher the aerosol layer, the stronger the path shortening effect, the larger the L2 bias magnitude (e.g., row 3 vs. 7, Table 2). Path shortening also applies to XCO_2, which is co-retrieved in the retrieval with 425 ppm ground truth. The bias is -1.2 ppm XCO_2 on average, with extreme values of -18.3 ppm (plume) and -15.8 ppm (background), demonstrating the working principle of the CO_2 proxy method. XCO_2 from SCIAMACHY was indeed found to vary by up to 37 ppm over the Sahara due to mineral dust aerosol (Houweling et al., 2005).

Figure 5 furthermore shows a moderate correlation between albedo and XCH_4 for both plume and background pixels. A higher albedo indicates a stronger contribution of direct surface reflected radiance relative to the scattered radiance (surface coupling). For higher surface coupling, path shortening is less prominent and the L2 bias magnitude is smaller compared to measurements with lower albedo. This correlation is really associated with an interplay between surface coupling and path shortening. For example, the path shortening mechanism leads to particularly strong L2 bias when, additionally to a high ALH (clearly above the peak methane concentration, >1500 m), the albedo is low (<0.2, e.g. rows 2, 4, 5 in Table 3).

For lower ALH, therefore, the aerosol would be located nearer to the maximum trace gas retrieval sensitivity near the ground, and path shortening would be reduced. This was confirmed with a separate MCS using a mean/STD for ALH of 1000 m/700 m, while mean/STD of ALW remained at 700 m/400 m. The MAE decreased to 1.29 $ppbCH_4$ and 0.25 $ppbCH_4$ for the lidar-constrained SRTM and NSRTM, respectively (scenario 4, Table 3).

Since the single scattering simulation scheme used here does not model multiple scattering, which would also allow path lengthening and thus a positively biased XCH_4, the true XCH_4 forms a hard upper limit and the distribution appears truncated (Figs. 3a). The degree of truncation depends on the measurement altitude. When the latter was moved downward, e.g., at 5 km above ground level, practically simulating an airborne geometry, the likelihood of aerosol layers being located above the sensor increased. For these cases, the scattered radiance contribution decreased, while surface coupling increased and positive bias became more likely, especially for high albedo (>0.3), leading to a more symmetrical L2 distribution (as already visible in Fig. 4b).

As they are drawn from a normal distribution, OC are roughly equally likely for plume and background and therefore positive and negative L2 biases have equal likelihood too. As a result, ΔXCH_4 and L3 bias distribution are symmetric (Figs. 3a, 4a).

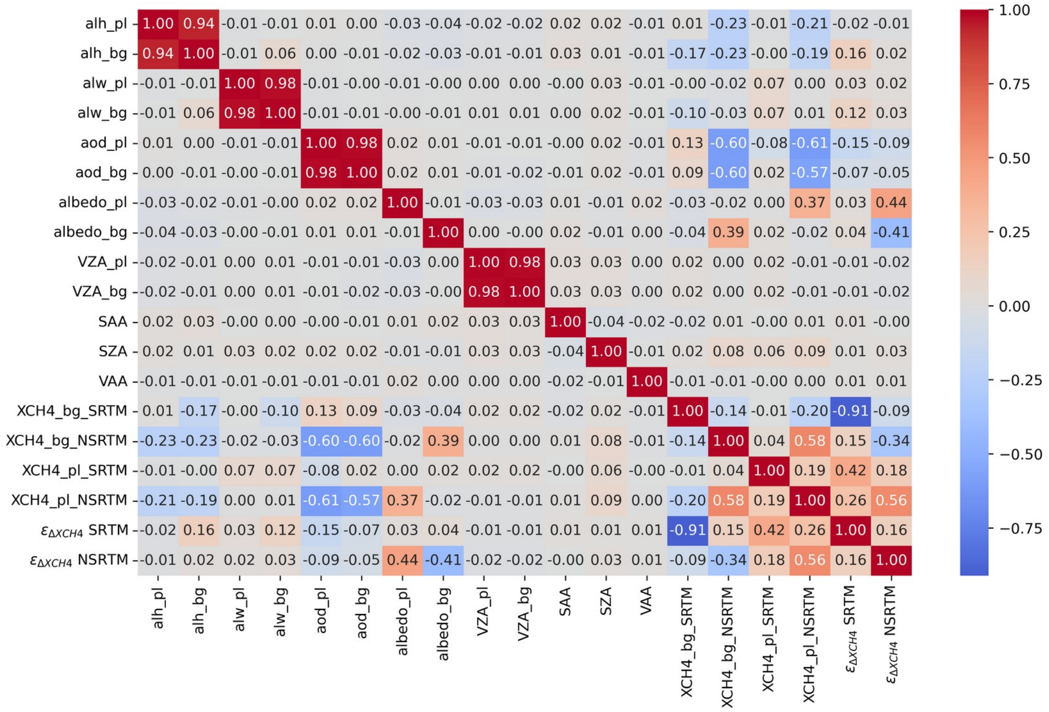

	alh_pl	alh_bg	alw_pl	alw_bg	aod_pl	aod_bg	albedo_pl	albedo_bg	VZA_pl	VZA_bg	SAA	SZA	VAA	XCH4_bg_SRTM	XCH4_bg_NSRTM	XCH4_pl_SRTM	XCH4_pl_NSRTM	$\varepsilon_{\Delta XCH4}$ SRTM	$\varepsilon_{\Delta XCH4}$ NSRTM
alh_pl	1.00	0.94	-0.01	-0.01	0.01	0.00	-0.03	-0.04	-0.02	-0.02	0.02	0.02	-0.01	0.01	-0.23	-0.01	-0.21	-0.02	-0.01
alh_bg	0.94	1.00	-0.01	0.06	0.00	-0.01	-0.02	-0.03	-0.01	-0.01	0.03	0.01	-0.01	-0.17	-0.23	-0.00	-0.19	0.16	0.02
alw_pl	-0.01	-0.01	1.00	0.98	-0.01	-0.00	-0.01	-0.00	0.00	0.00	-0.00	0.03	-0.01	-0.00	-0.02	0.07	0.00	0.03	0.02
alw_bg	-0.01	0.06	0.98	1.00	-0.01	-0.01	-0.00	-0.01	0.01	0.01	0.00	0.02	-0.01	-0.10	-0.03	0.07	0.01	0.12	0.03
aod_pl	0.01	0.00	-0.01	-0.01	1.00	0.98	0.02	0.01	-0.01	-0.01	-0.00	0.02	-0.01	0.13	-0.60	-0.08	-0.61	-0.15	-0.09
aod_bg	0.00	-0.01	-0.00	-0.01	0.98	1.00	0.02	0.01	-0.01	-0.02	-0.01	0.02	-0.01	0.09	-0.60	0.02	-0.57	-0.07	-0.05
albedo_pl	-0.03	-0.02	-0.01	-0.00	0.02	0.02	1.00	-0.01	-0.03	-0.03	0.01	-0.01	0.02	-0.03	-0.02	0.00	0.37	0.03	0.44
albedo_bg	-0.04	-0.03	-0.00	-0.01	0.01	0.01	-0.01	1.00	0.00	-0.00	0.02	-0.01	0.00	-0.04	0.39	0.02	-0.02	0.04	-0.41
VZA_pl	-0.02	-0.01	0.00	0.01	-0.01	-0.01	-0.03	0.00	1.00	0.98	0.03	0.03	0.00	0.02	0.00	0.02	-0.01	-0.01	-0.02
VZA_bg	-0.02	-0.01	0.00	0.01	-0.01	-0.02	-0.03	-0.00	0.98	1.00	0.03	0.03	0.00	0.02	0.00	0.02	-0.01	-0.01	-0.02
SAA	0.02	0.03	-0.00	0.00	-0.00	-0.01	0.01	0.02	0.03	0.03	1.00	-0.04	-0.02	-0.02	0.01	-0.00	0.01	0.01	-0.00
SZA	0.02	0.01	0.03	0.02	0.02	0.02	-0.01	-0.01	0.03	0.03	-0.04	1.00	-0.01	0.02	0.08	0.06	0.09	0.01	0.03
VAA	-0.01	-0.01	-0.01	-0.01	-0.01	-0.01	0.02	0.00	0.00	0.00	-0.02	-0.01	1.00	-0.01	-0.01	-0.00	0.00	0.01	0.01
XCH4_bg_SRTM	0.01	-0.17	-0.00	-0.10	0.13	0.09	-0.03	-0.04	0.02	0.02	-0.02	0.02	-0.01	1.00	-0.14	-0.01	-0.20	-0.91	-0.09
XCH4_bg_NSRTM	-0.23	-0.23	-0.02	-0.03	-0.60	-0.60	-0.02	0.39	0.00	0.00	0.01	0.08	-0.01	-0.14	1.00	0.04	0.58	0.15	-0.34
XCH4_pl_SRTM	-0.01	-0.00	0.07	0.07	-0.08	0.02	0.00	0.02	0.02	0.02	-0.00	0.06	-0.00	-0.01	0.04	1.00	0.19	0.42	0.18
XCH4_pl_NSRTM	-0.21	-0.19	0.00	0.01	-0.61	-0.57	0.37	-0.02	-0.01	-0.01	0.01	0.09	0.00	-0.20	0.58	0.19	1.00	0.26	0.56
$\varepsilon_{\Delta XCH4}$ SRTM	-0.02	0.16	0.03	0.12	-0.15	-0.07	0.03	0.04	-0.01	-0.01	0.01	0.01	0.01	-0.91	0.15	0.42	0.26	1.00	0.16
$\varepsilon_{\Delta XCH4}$ NSRTM	-0.01	0.02	0.02	0.03	-0.09	-0.05	0.44	-0.41	-0.02	-0.02	-0.00	0.03	0.01	-0.09	-0.34	0.18	0.56	0.16	1.00

Figure 5. Pearson cross correlation matrix for the MCS parameters for the lidar scenario (section 4.1). There are moderate correlations between independently calculated variables, and thus are non-causal, such as between plume pixel albedo and background XCH_4. Since the L3 error is the difference between the retrieved and the true L3 enhancement (Eq. (4)), which is fixed at 30 ppbCH_4, the L3 bias correlates (anti-correlates) with the plume (background) XCH_4 for both NSRTM and SRTM. Weak correlation values (<0.4) may indicate multi-parameter dependence, which is not fully captured by pairwise Pearson correlations.

A strong L2 bias, e.g., due to high ALH, and/or low albedo and thus low surface coupled radiance, alone does not cause a large L3 bias magnitude, if plume and background albedo are comparable (within ~50%) and/or AOD is low (e.g., rows 3, 9, 10 in Table 2). If, however, due to different OC, path-shortening and surface coupling work disproportionally for plume and background, the L2 bias inequality increases and, as a result, the L3 bias magnitude increases (Eq. (4)). This effect is promoted by high AOD and ALH (Figs. 6a and b), i.e., strong path-shortening. Due to the assumption of a smoothly varying aerosol layer, plume and background ALW, AOD and ALH strongly correlate, and plume/background albedo contrast is the strongest driver of L2 bias inequality and thus L3 bias (Fig. 6c), while VZA differences have little impact and VAA per default are equal for plume and background. For instance, if the plume pixel albedo is lower than the background albedo, plume XCH_4 is more negatively biased than background XCH_4, and, with Eq. (2), L3 bias is negative (e.g., row 2 in Table 2). A positive L3 bias would be associated with a plume surface albedo larger than background albedo (e.g., rows 4, 5 in Table 2). Therefore, differences in OC drive the L3 bias magnitude, which relates to the core hypothesis.

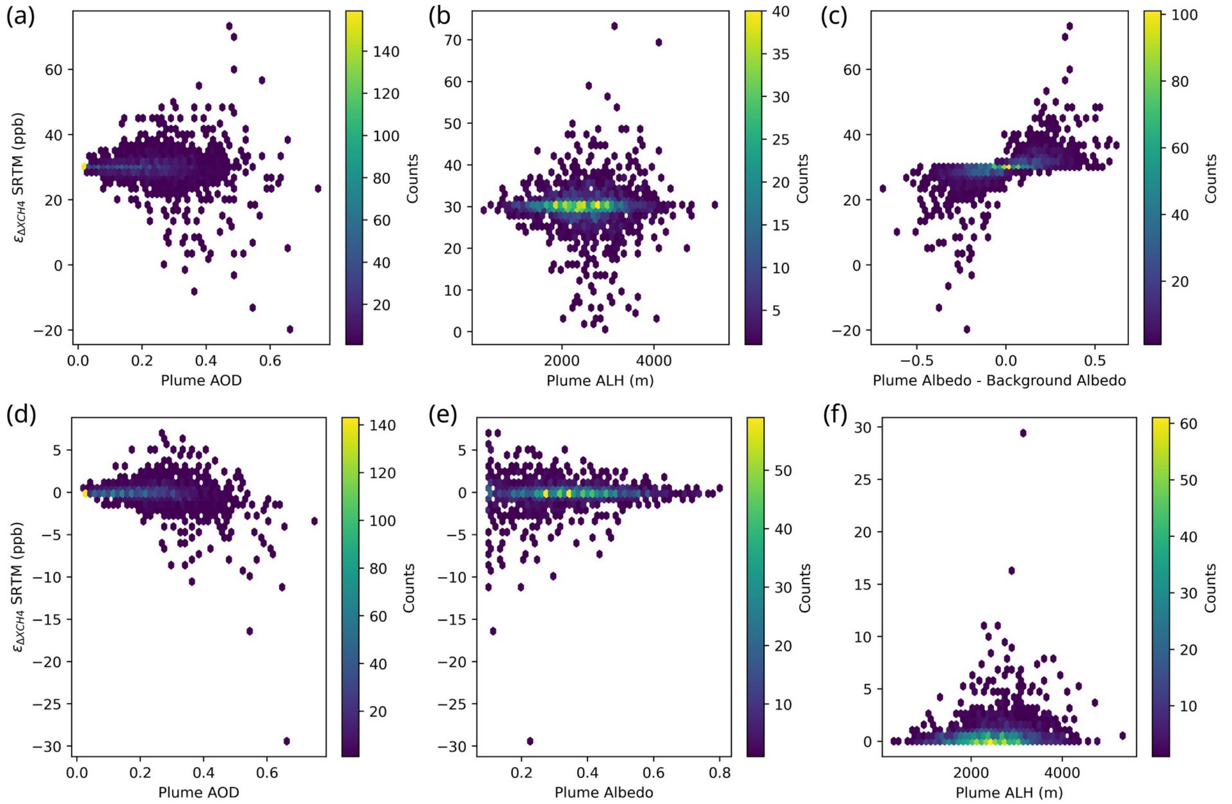

Figure 6. Scatter plots color coded for occurrence showing L3 bias against different MCS parameters. (a) to (c): for the lidar scenario for NSRTM (scenario 1, Table 3) (a) AOD. (b) plume/background albedo contrast. (c) ALH. (d) to (f): Scatter plot for the NSRTM case for scenario 5 in Table 3 (with equal albedo for plume and background). (a) AOD, (b) albedo (c) ALH. Only plume parameters are shown, since plume and background aerosol parameters are strongly correlated.

As will be investigated in more detail in the following, L2 bias inequality occurs even for equal OC and reasonably similar aerosol profiles, but is amplified by difference in aerosol profile parameters, and more so, OC differences between plume and background. To further isolate governing mechanisms and provide further testing evidence for the null-hypothesis, three reduced complexity tests were carried out. The SRTM was ideally constrained for all three. This means, while still random, the retrieval aerosol profile parameters (ALH, ALW, AOD) were equal to the true values for both plume and background.

For the first reduced complexity scenario, OC (albedo, VZA, VAA) were identical for plume and background. As the SRTM was constrained with the true aerosol profiles, the corresponding MAE is ~0 (scenario 5, Table 3). The L2 bias distribution is nearly delta-like for both plume and background, and L3 bias is ~0 for all measurements. For the NSRTM, the MAE reduced from 2.57 ppbCH$_4$ to 0.69 ppbCH$_4$, with L3 bias ranging between about -11 and 4 ppbCH_4. Despite equal OC, the non-zero MAE of 0.69 ppbCH_4 implies that a number of measurements entailed cases with a plume/background L2 bias inequality, caused by plume/background difference in aerosol profile. For these measurements, albedo was low (<0.2) and/or AOD was high (Figs. 6d and e), i.e., radiance surface coupling was weak. This increased the sensitivity of the retrieval to aerosol-induced path shortening, causing small differences in effective optical path between plume and background (e.g. different ALH) to map into disproportionate L2 biases and thus higher L3 bias. As before, XCH_4 and ALH anticorrelated for plume and background, meaning large ALH and large ALH differences promoted higher L3 bias (Fig. 6f). No notable dependence on ALW was found.

The second reduced complexity scenario (scenario 6, Table 3) was identical to the first (equal OC, true aerosol profile for retrieval), except that differences in aerosol profile were removed. The same aerosol profile was used for plume and background. The MAE for the SRTM was ~0 again, as expected. For the NSRTM, min/max L2 bias was -31 ppbCH_4/-0.3 ppbCH_4 (plume) and -30.4 ppbCH_4/-0.3 ppbCH_4 (background) and the MAE was 0.09 ppbCH_4. This small MAE confirms the trivial case of canceling L2 bias (Eq. (3)) due to equal aerosol profiles for plume and background, if OC are the same. Methane does not contribute to scattering. However, differences in methane VCD between plume and background modify the attenuation of scattered photons (Eq. 6 in supporting information), leading to plume/background differences in the relative contribution of scattered radiance to the total signal. This explains small L2 bias inequalities and thus non-zero (sub-ppb) L3 bias even in this case.

The third run was identical to the second run (constant aerosol), but OC differed again (scenario 7, Table 3). MAE was 2.5 ppbCH_4, i.e., similar to the MAE with a varying aerosol profile (e.g. scenario 1, Table 3). This indicates that aerosol profile differences do indeed amplify L3 bias, but less so than differences in OC, which in this study practically means albedo.

In summary, the reduced complexity tests show that for identical aerosol profiles for plume and background and OC (mainly albedo), the radiative transfer is more similar for both. As a consequence, the associated L2 biases approximately cancel, leading to a low L3 bias magnitude. As the aerosol profile varies between plume and background, differences in path length, scattering phase function and radiance surface coupling increase, and cause noticeable L3 biases for most measurements. These effects are further enhanced once OC between plume and background differ. The assumption of canceling L2 biases (Eqs. (2) and (3)) does no longer hold as soon as OC differ, regardless if the aerosol profile is constant or varying between plume and background.

Overall, the result suggest that a constrained SRTM becomes more useful the more OC, most importantly albedo, differ between plume and background. This is likely the case, given the GSD of least 50 m, plume dimensions of hundreds of meters and a lidar footprint of ~130 m (Fig. 1b)

5.2.2 Bias mechanisms for the SRTM

As noted above, 0.4% of lidar-constrained measurements still exhibit L2 bias magnitudes ≥5 ppbCH_4, with plume (background) L2 biases ranging from −7 to 13 ppbCH_4 (−4 to 3 ppbCH_4). These are associated with large differences between retrieval and background aerosol profiles.

The same principal mechanisms that govern L3 bias for the NSRTM (surface coupling vs. path shortening) are at play, but they become pronounced more the poorer the SRTM is constrained. In the physics-based retrieval framework used here, the aerosol vertical profile (AOD, ALH, ALW) is fixed, which may lead to path-length mismatches. Trace gas VCD and surface albedo are the only adjustable state-vector elements. Hence, L2 bias, and therefore L3 bias, are partly driven by how close retrieval and true aerosol profiles are. For instance, if the retrieval ALH is higher than the true ALH (measured spectra with deeper methane absorption features than explainable with fixed aerosol profile), forward modeled path shortening is overestimated, which is compensated by increasing model VCD, causing positive XCH_4 bias. AOD mismatch also contributes and is more pronounced for higher AOD. This mechanism likely contributed to a slight asymmetry around the true XCH_4 for both plume and background (Fig. 4a), with large positive L2 bias occurring more frequently than large negative L2 bias. The larger errors of aerosol profile parameters explain the higher occurrence of larger XCH_4 biases for the background and thus the broader distribution (SRTM, Fig. 3a).

A loosely constrained SRTM, therefore, performs equally poor as a NSRTM, such as shown with the random guess scenario (Fig. 4). For both NSRTM and SRTM, relatively large L2 biases of tens of $ppbCH_4$ occur, with values between about -32 and 50 $ppbCH_4$ (Fig. 4a). L2 bias approximately canceled when the retrieval aerosol profile was relatively close to the true aerosol profile, but led to large L3 bias otherwise, particularly in combination with high plume/background albedo differences. Largely overestimated ALH in the SRTM caused overestimated path shortening, corresponding to an AK with misallocated sensitivity, leading to overestimated (positively biased) XCH_4, which was amplified for high plume/background albedo contrast. On the contrary, for measurements with stronger surface coupling (albedo >0.2, AOD <0.2), aerosol scattering less dominated the TOA radiance and aerosol profile errors had a lower impact on the averaging kernel. Depending on the OC, we found that ALH accuracy should be a few hundred meters in order for the L3 bias magnitude to remain <10 $ppbCH_4$ (< 30% of enhancement).

5.4 Other limitations of the simulation scheme

The relationship between the discussed aerosol-induced mechanisms and the L2 and L3 biases depend to some extent on the retrieval model and its limitations. For example, Huang et al. (2020) found that, depending on the retrieval model used, the L3 bias was either independent on XCH_4 or it decreased with increasing XCH_4. Here, we found that L2 bias remained almost constant (0.05 ppb decrease for 10 ppb reduction in true ΔXCH_4) and L3 bias would remain ~2.6 $ppbCH_4$ even with lower CH_4 enhancements.

The forward modeling scheme used here was able to simulate a limited ensemble of processes only. For instance, multiple scattering was not modeled. Although representative, only a single aerosol type has been considered. The two-pixel assumption is another major simplification, which, however, allowed to focus on fundamental mechanisms to assess the principle suitability of a aerosol profile from lidar to constrain the retrieval model. However, even full-physics retrievals are limited (Frankenberg et al., 2025). In line with this study, more complex simulations of surface and atmospheric scattering also found that albedo induced bias is amplified with aerosol abundance, as observed in XCH_4 from TROPOMI (Somkuti et al., 2025).

Being sampled independently, the MCS entailed less likely combinations of aerosol parameters, such as AOD and ALW. However, these represent values from the tails of the distribution. While they would not alter the main results, they helped to unravel the mechanism of the model. For example, an AOD of 0.02 and ALW of 758 m (row 9, Table 2) would correspond to practically clear air, rather than the intended dust aerosol scenario. Further, the lidar would neither be measuring any signal nor be needed in that case, consistent with the discussion above.

The finding that albedo difference is the dominating driver of L3 bias over aerosol profile differences is based on a smoothly varying layer (mean difference 205 m/62 m/0.02 for ALH, ALW and AOD). For strongly varying aerosol layers, such as a cloud edge, large L3 bias would arise even at equal albedo. This has been assessed in a stratus cloud MCS (Queißer et al., 2026).

Due to computational constraints, the vertical grid spacing was 1000 m, as in a real data processing. This led to under-sampling of some aerosol ALW, thus contributing to a flattening of the relationship with ALW. However, repeating the lidar MCS using 250 m grid spacing yielded the same MAE and differences in XCH_4 were <0.05%.

6 Conclusions

The potential to constrain a physics based methane retrieval scheme for space-borne imaging spectroscopy with aerosol layer height and width (ALH, ALW) from lidar was assessed. The enhancement (ΔXCH_4, plume) is retrieved as the difference between the XCH_4 of the plume pixels and the XCH_4 at the background pixels next to the plume. The hypothesis was tested that knowledge of the aerosol profile from a single staring lidar, probing the plume only (assumed to be at swath center), would not be beneficial to reduce the bias of the methane Level-3 (L3) results ΔXCH_4, since it would miss aerosol profile at the background area of a given scene. In the case of a constant aerosol profile for plume and background, the Level-2 (L2) biases of plume and background would possibly cancel, leading to nil L3 bias and a lidar would be redundant.

To test the hypothesis, end-to-end processing was performed in Monte Carlo simulation (MCS) mode with 2000 retrievals from simulated TOA spectra up to L2 (XCH_4) and L3 (ΔXCH_4) using a non-scattering RTM (NSRTM, ignoring aerosol extinction) and a scattering RTM (SRTM, accounting for aerosol extinction assuming single scattering). A transported mineral dust layer was assumed, covering the complete scene, smoothly transitioning between plume and background, represented by a single pixel each. Based on the results, the following main conclusions are drawn:

(a) For equal OC, notably albedo, and constant aerosol profile between plume and background, the L2 bias for plume/background is approximately equal and cancels, leading to small L3 bias in most cases (<< 1 $ppbCH_4$), even without correcting for aerosol (scenario 6, Table 3).

(b) For different OC, significant L2 bias inequalities may arise, caused by a combination of path-shortening and surface coupling, with L3 bias values of several tens of $ppbCH_4$ for a NSRTM or a poorly constrained SRTM, regardless if the aerosol profile varies between plume and background or not.

(c) Therefore, plume/background L2 bias does generally not cancel if plume/background OC, notably albedo, differ.

(d) A (lidar-) constrained SRTM is effective for high albedo contrast, even for a smooth to constant aerosol profile, such as an extended mineral dust layer; and even for homogeneous albedo, if albedo is low, AOD and ALH are high and plume/background aerosol variations are high (Table 3).

(e) In the MCS, a lidar-constraint SRTM with AOD uncertainty <10% reduced the L2 bias and L2 bias inequality and thus L3 bias for most of the 2000 measurements (L3 MAE ~0.5 ppbCH_4 with min/max L3 bias of -14.9/6.3 ppbCH_4). The occurrence of large L3 bias ($\geq$5 ppbCH_4 or ~17% of enhancement), which, to first order, would propagate to a L4 (flux) error of $\geq$17%, is reduced from 13.5% to 0.4%. This refutes the null hypothesis.

(f) ALH accuracy must be a few hundred meters for L3 bias magnitudes to remain <10 ppbCH_4 (i.e., <30% of ΔXCH_4)

(g) AOD needs to be known better than 50% for a lidar-constraint SRTM to be efficient (supporting information, text S2)

(h) Third party aerosol profile data may complement lidar retrievals, for instance, if lidar soundings fail.

If AOD cannot be inverted from lidar data, it could be retrieved from observational networks such as AERONET (Holben et al., 1998) or L2 data from EarthCare (Wandinger et al., 2023). For further reaching conclusions, a more detailed assessment on spatio-temporal coverage and availability and accuracy of such data is needed.

In the model used here, MAE was found to vary very little with ΔXCH_4. Since L4 bias to first order scales with the L3 bias, this suggests, therefore, that aerosol bias correction with lidar data would be particularly beneficial for smaller ΔXCH_4 and hence smaller fluxes (<100 kg$CH_4$$h^{-1}$) or higher diluted plumes. More leaks could be detected and more plumes could be quantified. In the US oil and gas sector ~70% of the methane sources emit less than 100 kg$CH_4$$h^{-1}$ (Williams et al., 2025). Of course, this is provided that the sensitivity of the instrument-retrieval system is sufficient to resolve those smaller enhancements.

In summary, the study suggests that, given an extended mineral dust aerosol layer, a single lidar profile is beneficial for space-borne methane plume quantification, especially for large albedo contrast between plume and background scene pixels, as they may arise in reality (Fig. 1). The result informs next steps, which will include high altitude measurements to validate the benefit of the aerosol lidar in methane remote sensing.

Since CO_2 is co-retrieved and proportionally biased by aerosol, CO_2 plume quantification would equally benefit especially in areas where other aerosol-correction methods, such as the proxy method, fail. There are implications beyond man-made methane or CO_2 emissions. For instance, volcanic aerosols, including sulfur species, are a major constituent of magmatic degassing of CO_2. A lidar constrained retrieval could allow retrieving more accurate CO_2 fluxes, and in combination with a full physics retrieval, possibly a more accurate retrieval of volcanic aerosol properties, such as aerosol layer height (Theys et al., 2022). This could allow a more accurate quantification of the geological carbon cycle (Werner et al., 2019).

Acknowledgments

The authors would like to thank Jochen Landgraf, who provided major input to the fixed-aerosol profile retrieval notion, and Herbert Nett and Sean Crowell for their ongoing support and valuable contribution. The project received funding from the ESA InCubed programme (ESA Contract No. 4000141570/23/I-DTO) and from Luxembourg Space Agency (Contract No. 4000144851/24/NL/VR).

Data Availability Statement

The data supporting the results of this study are publicly available in Zenodo (Queißer et al., 2026). The repository includes all Monte Carlo simulation (MCS) results presented in this paper, including NetCDF output files, figures, and Python scripts used to reproduce the simulations and figures. The dataset further includes the original OPAC aerosol input files and derived NetCDF parameter files, along with Python scripts for reading them and generating aerosol profiles for the E2E framework. It also contains aerosol optical depth (AOD) bias test cases and associated run files. The E2E framework used in this study is based on the SRON open-source Toolbox for End-to-End Simulations (TEDS), available at https://teds.readthedocs.io/en/latest (TEDS, 2026). The full end-to-end and lidar simulation framework contains proprietary components and is not publicly available due to intellectual property restrictions. However, the supporting information includes key information required to reproduce the results presented in this study. Aerosol optical properties, including single scattering albedo and scattering phase functions, were taken from the OPAC database (Hess et al., 1998) available at https://geisa.aeris-data.fr/opac. Aerosol layer properties (ALH, ALW, and AOD) were obtained from the AERONET observational network (Holben et al., 1998), available at https://aeronet.gsfc.nasa.gov.

Conflict of Interest Disclosure

The authors declare there are no conflicts of interest for this manuscript

References

Bösch, H., Toon, G. C., Sen, B., Washenfelder, R. A., Wennberg, P. O., Buchwitz, M., de Beek, R., Burrows, J. P., Crisp, D., Christi, M., Connor, B. J., Natraj, V., & Yung, Y. L. (2006). Space-based near-infrared CO_2 measurements: Testing the Orbiting Carbon Observatory retrieval algorithm and validation concept using SCIAMACHY observations over Park Falls, Wisconsin. *J. Geophys. Res.*, 111, D23302. https://doi.org/10.1029/2006JD007080

Butz, A., Galli, A., Hasekamp, O., Landgraf, J., Tol, P., & Aben, I. (2012). TROPOMI aboard Sentinel-5 Precursor: Prospective performance of CH4 retrievals for aerosol and cirrus loaded atmospheres. *Remote Sens. Environ.*, 120, 267–276. https://doi.org/10.1016/j.rse.2011.05.030

Chan Miller, C., Roche, S., Wilzewski, J. S., Liu, X., Chance, K., Souri, A. H., Conway, E., Luo, B., Samra, J., Hawthorne, J., Sun, K., Staebell, C., et al. (2024). Methane retrieval from MethaneAIR using the CO_2 proxy approach. *Atmos. Meas. Tech.*, 17, 5429–5454. https://doi.org/10.5194/amt-17-5429-2024

Coddington, O. M., Richard, E. C., Harber, D., Pilewskie, P., Woods, T. N., Chance, K., et al. (2021). The TSIS-1 hybrid solar reference spectrum. *Geophys. Res. Lett.*, 48, e2020GL091709. https://doi.org/10.1029/2020GL091709

Dandenault, P. B., Dao, E., Kaeppler, S. R., & Miller, E. S. (2020). Estimation of human-error contributions to historical ionospheric data. *Earth Space Sci.*, 7, e2020EA001123. https://doi.org/10.1029/2020EA001123

Deschamps, A., Marion, R., Briottet, X., & Foucher, P.-Y. (2013). Simultaneous retrieval of CO2 and aerosols in a plume from hyperspectral imagery: Application to the characterization of forest fire smoke using AVIRIS data. *Int. J. Remote Sens.*, 34(19), 6837–6864. https://doi.org/10.1080/01431161.2013.809499

Di Martino, R. M. R., Gurrieri, S., Paonita, A., et al. (2024). Unveiling spatial variations in atmospheric CO2 sources: A case study of metropolitan area of Naples, Italy. *Sci. Rep.*, 14, 20483. https://doi.org/10.1038/s41598-024-71348-9

Dubovik, O., Herman, M., Holdak, A., Lapyonok, T., Tanré, D., Deuzé, J. L., Ducos, F., Sinyuk, A., & Lopatin, A. (2011). Statistically optimized inversion algorithm for enhanced retrieval of aerosol properties from spectral multi-angle polarimetric satellite observations, *Atmos. Meas. Tech.*, 4, 975–1018, https://doi.org/10.5194/amt-4-975-2011

Duren, R., Cusworth, D., Ayasse, A., Howell, K., Diamond, A., Scarpelli, T., Kim, J., O’Neill, K., Lai-Norling, J., Thorpe, A., Zandbergen, S. R., Shaw, L., et al. (2025). The Carbon Mapper emissions monitoring system. *EGUsphere* preprint. https://doi.org/10.5194/egusphere-2025-2275

European Space Agency. (2020). *Copernicus CO₂ Monitoring Mission Requirements Document (MRD)*, Issue 3.0, Reference EOP-SM/3088/YM-ym. Earth and Mission Science Division, ESA.

Frankenberg, C., Hasekamp, O., O'Dell, C., Sanghavi, S., Butz, A., & Worden, J. (2012). Aerosol information content analysis of multi-angle high spectral resolution measurements and its benefit for high accuracy greenhouse gas retrievals. *Atmos. Meas. Tech.*, 5, 1809–1821. https://doi.org/10.5194/amt-5-1809-2012

Frankenberg, C., Platt, U., & Wagner, T. (2005). IMAP-DOAS for strongly absorbing trace gases. *Atmos. Chem. Phys.*, 5, 9–22. https://doi.org/10.5194/acp-5-9-2005

Frankenberg, C., Sanghavi, S., Saha, A., Wennberg, P. O., Jacob, D. J., & Michalak, A. M. (2025). On the use of N2O as a light-path proxy for accurate greenhouse gas measurements from space. *Geophys. Res. Lett.*, 52, e2024GL114131. https://doi.org/10.1029/2024GL114131

Gerilowski, K., Tretner, A., Krings, T., Buchwitz, M., Bertagnolio, P. P., Belemezov, F., Erzinger, J., Burrows, J. P., & Bovensmann, H. (2011). MAMAP spectrometer system. *Atmos. Meas. Tech.*, 4, 215–243. https://doi.org/10.5194/amt-4-215-2011

Gordon, I. E., Rothman, L. S., Hargreaves, R. J., Hashemi, R., Karlovets, E. V., Skinner, F. M., et al. (2022). The HITRAN2020 database. *J. Quant. Spectrosc. Radiat. Transfer*, 277, 107949. https://doi.org/10.1016/j.jqsrt.2021.107949

Guanter, L., Kaufmann, H., Segl, K., Foerster, S., Rogass, C., Chabrillat, S., Kuester, T., Hollstein, A., Rossner, G., Chlebek, C., Straif, C., et al. (2015). The EnMAP mission. *Remote Sens.*, 7, 8830–8857. https://doi.org/10.3390/rs70708830

Hess, M., Koepke, P., and Schult, I. (1998), Optical Properties of Aerosols and Clouds: The Software Package OPAC, Bull. Amer. Meteorol. Soc., **79**, 831–844, https://doi.org/10.1175/1520-0477(1998)079\<0831:OPOAAC>2.0.CO;2.

Holben, B. N., Eck, T. F., Slutsker, I., Tanré, D., Buis, J. P., Setzer, A., Vermote, E., Reagan, J. A., Kaufman, Y. J., Nakajima, T., Lavenu, F., Jankowiak, I., & Smirnov, A. (1998). AERONET—A federated instrument network and data archive for aerosol characterization. *Remote Sens. Environ.*, *66*(1), 1–16. https://doi.org/10.1016/S0034-4257(98)00031-5

Houweling, S., Hartmann, W., Aben, I., Schrijver, H., Skidmore, J., Roelofs, G.-J., & Breon, F.-M. (2005). Evidence of systematic errors in SCIAMACHY-observed CO2 due to aerosols, *Atmos. Chem. Phys.*, 5, 3003–3013, https://doi.org/10.5194/acp-5-3003-2005.

Huang, Y., Natraj, V., Zeng, Z.-C., Kopparla, P., & Yung, Y. L. (2020). Quantifying the impact of aerosol scattering on the retrieval of methane from airborne remote sensing measurements. *Atmos. Meas. Tech.*, 13, 6755–6769. https://doi.org/10.5194/amt-13-6755-2020

Jacob, D. J., Varon, D. J., Cusworth, D. H., Dennison, P. E., Frankenberg, C., Gautam, R., Guanter, L., Kelley, J., McKeever, J., Ott, L. E., Poulter, B., Qu, Z., Thorpe, A. K., Worden, J. R., & Duren, R. M. (2022). Quantifying methane emissions from the global scale down to point sources using satellite observations of atmospheric methane. *Atmos. Chem. Phys.*, 22, 9617–9646. https://doi.org/10.5194/acp-22-9617-2022

Jänicke, L. K., Preusker, R., Docter, N., & Fischer, J. (2023). Estimation of aerosol layer height from OLCI measurements in the O2A-absorption band over oceans. *Remote Sens.*, 15(16), 4080. https://doi.org/10.3390/rs15164080

Kim, H., Chen, X., Wang, J., Lu, Z., Zhou, M., Carmichael, G., Park, S. S., & Kim, J. (2024). Aerosol layer height (ALH) retrievals from oxygen absorption bands: Intercomparison and validation among different satellite platforms, GEMS, EPIC, and TROPOMI. *EGUsphere* [preprint]. https://doi.org/10.5194/egusphere-2023-3115

Klausner, T., Mertens, M., Huntrieser, H., Galkowski, M., Kuhlmann, G., Baumann, R., Fiehn, A., Jöckel, P., Pühl, M., & Roiger, A. (2020). Urban greenhouse gas emissions from the Berlin area: A case study using airborne CO2 and CH4 in situ observations in summer 2018. *Elementa: Sci. Anthropocene*, 8, 15. https://doi.org/10.1525/elementa.411

Krings, T., Gerilowski, K., Buchwitz, M., Reuter, M., Tretner, A., Erzinger, J., Heinze, D., Pflüger, U., Burrows, J. P., & Bovensmann, H. (2011). MAMAP – a new spectrometer system for column-averaged methane and carbon dioxide observations from aircraft: Retrieval algorithm and first inversions for point source emission rates. *Atmos. Meas. Tech.*, 4, 1735–1758. https://doi.org/10.5194/amt-4-1735-2011

Landgraf, J., Butz, A., Hasekamp, O., Hu, H., & aan de Brugh, J. (2019). *Sentinel 5 L2 Prototype Processors, Algorithm Theoretical Baseline Document: Methane Retrieval*, SRON-ESA-S5L2PP-ATBD-001-v3.1. SRON Netherlands Institute for Space Research, Utrecht, The Netherlands.

Levelt, P. F., van den Oord, G. H. J., Dobber, M. R., Malkki, A., Visser, H., de Vries, J., Stammes, P., Lundell, J. O. V., & Saari, H. (2006). The ozone monitoring instrument. *IEEE Trans. Geosci. Remote Sens.*, 44, 1093–1101. https://doi.org/10.1109/TGRS.2006.872333

Lyapustin, A., Wang, Y., Laszlo, I., Kahn, R., Korkin, S., Remer, L., et al. (2011). Multiangle implementation of atmospheric correction (MAIAC): 2. Aerosol algorithm. *J. Geophy. Res.*, 116(D3), D03211. https://doi.org/10.1029/2010JD014986

MacLean, J.-P. W., M. Girard, D. Jervis, D. Marshall, J. McKeever, A. Ramier, M. Strupler, E. Tarrant, and D. Young (2024), Offshore methane detection with GHGSat. *Atmos. Meas. Tech.*, 17, 863–874, https://doi.org/10.5194/amt-17-863-2024

Milford, C., Cuevas, E., Marrero, C., Bustos, J., Gallo, V., Rodríguez, S., Romero-Campos, P., & Torres, C. (2019). Impacts of desert dust outbreaks on air quality in urban areas. *Atmosphere*, 11, 23. https://doi.org/10.3390/atmos11010023

Noël, S., Buchwitz, M., Hilker, M., Reuter, M., Weimer, M., Bovensmann, H., Burrows, J. P., Bösch, H., & Lang, R. (2024). Greenhouse gas retrievals for the CO2M mission using the FOCAL method: First performance estimates. *Atmos. Meas. Tech.*, 17, 2317–2334. https://doi.org/10.5194/amt-17-2317-2024

O'Dell, C. W., Connor, B., Bösch, H., O'Brien, D., Frankenberg, C., Castano, R., Christi, M., Eldering, D., Fisher, B., Gunson, M., McDuffie, J., Miller, C. E., Natraj, V., Oyafuso, F., Polonsky, I., Smyth, M., Taylor, T., Toon, G. C., Wennberg, P. O., & Wunch, D. (2012). The ACOS CO2 retrieval algorithm – Part 1: Description and validation against synthetic observations. *Atmos. Meas. Tech.*, 5, 99–121. https://doi.org/10.5194/amt-5-99-2012

Queißer, M., Thomás, S. T. M., Vilaseca, D., Armandillo, E., & Stepanova, D. (2026). MCS scenario results [Data set]. *Zenodo*. https://doi.org/10.5281/zenodo.19708312

Ratcliffe, N. G., Ryder, C. L., Bellouin, N., Woodward, S., Jones, A., Johnson, B., Wieland, L.-M., Dollner, M., Gasteiger, J., & Weinzierl, B. (2024). Long-range transport of coarse mineral dust: An evaluation of the Met Office Unified Model against aircraft observations. *Atmos. Chem. Phys.*, 24, 12161–12181. https://doi.org/10.5194/acp-24-12161-2024

Schepers, D., Guerlet, S., Butz, A., Landgraf, J., Frankenberg, C., Hasekamp, O., Blavier, J.-F., Deutscher, N. M., Griffith, D. W. T., Hase, F., et al. (2012). Methane retrievals from Greenhouse Gases Observing Satellite (GOSAT) shortwave infrared measurements: Performance comparison of proxy and physics retrieval algorithms. *J. Geophys. Res.*, 117, D10. https://doi.org/10.1029/2011JD016124

Somkuti, P., McGarragh, G., O'Dell, C., Di Noia, A., Vogel, L., Crowell, S., Ott, L. E., and Bösch, H. (2025). Surface reflectance biases in XCH4 retrievals from the 2.3 μm band are enhanced in the presence of aerosols. *Atmos. Meas. Tech.*, 18, 4647–4663, https://doi.org/10.5194/amt-18-4647-2025.

Staebell, C., Sun, K., Samra, J., Franklin, J., Chan Miller, C., Liu, X., Conway, E., Chance, K., Milligan, S., & Wofsy, S. (2021). Spectral calibration of the MethaneAIR instrument. *Atmos. Meas. Tech.*, 14, 3737–3753. https://doi.org/10.5194/amt-14-3737-2021

Sugimoto, N., A. Shimizu, T. Nishizawa, Y. Jin, and K. Yumimoto (2020), Long-range-transported mineral dust from Africa and Middle East to East Asia observed with the Asian Dust and Aerosol Lidar Observation Network (AD-Net), *EPJ Web Conf.*, 237, 05009, https://doi.org/10.1051/epjconf/202023705009

Sun, J., Veefkind, P., Nanda, S., van Velthoven, P., & Levelt, P. (2019). The role of aerosol layer height in quantifying aerosol absorption from ultraviolet satellite observations. Atmos. Meas. Tech., 12, 6319–6340, https://doi.org/10.5194/amt-12-6319-2019, 2019.

TEDS (2026). Toolbox for End-to-enD Simulations. https://teds.readthedocs.io/en/latest, , last accessed 24/04/2026.

Thorpe, A. K., Green, R. O., Thompson, D. R., Brodrick, P. G., Chapman, J. W., Elder, C. D., Irakulis-Loitxate, I., Cusworth, D. H., Ayasse, A. K., Duren, R. M., Frankenberg, C., et al. (2023). Attribution of methane and CO_2 using EMIT. *Sci. Adv.*, 9, eadh2391. https://doi.org/10.1126/sciadv.adh2391

Tindan, J. Z., Jin, Q., & Pu, B. (2023). Understanding day–night differences in dust aerosols over the dust belt of North Africa, the Middle East, and Asia. *Atmos. Chem. Phys.*, 23, 5435–5466. https://doi.org/10.5194/acp-23-5435-2023

Theys, N., Lerot, C., Brenot, H., van Gent, J., De Smedt, I., Clarisse, L., Burton, M., Varnam, M., Hayer, C., Esse, B., & Van Roozendael, M. (2022). Improved retrieval of SO2 plume height from TROPOMI using an iterative covariance-based retrieval algorithm. *Atmos. Meas. Tech.*, 15, 4801–4817. https://doi.org/10.5194/amt-15-4801-2022

U.S. Standard Atmosphere. (1976). *U.S. Standard Atmosphere, 1976*. NASA-TM-X-74335, NOAA-S/T 76-1562, U.S. Government Printing Office, Washington, D.C. https://ntrs.nasa.gov/citations/19770009539

Wandinger, U., Haarig, M., Baars, H., Donovan, D., & van Zadelhoff, G.-J. (2023) Cloud top heights and aerosol layer properties from EarthCARE lidar observations: the A-CTH and A-ALD products. Atmos. Meas. Tech., 16, 4031–4052, https://doi.org/10.5194/amt-16-4031-2023

Werner, C., Fischer, T. P., Aiuppa, A., Edmonds, M., Cardellini, C., et al. (2019). Carbon dioxide emissions from subaerial volcanic regions: Two decades in review. In B. N. Orcutt, I. Daniel, & R. Dasgupta (Eds.), *Deep Carbon, Past to Present* (pp. 188–236). Cambridge University Press. https://doi.org/10.1017/9781108677950

Williams, J. P., Omara, M., Himmelberger, A., Zavala-Araiza, D., MacKay, K., Benmergui, J., Sargent, M., Wofsy, S. C., Hamburg, S. P., & Gautam, R. (2025). Small emission sources in aggregate disproportionately account for a large majority of total methane emissions from the US oil and gas sector. *Atmos. Chem. Phys.*, 25, 1513–1532. https://doi.org/10.5194/acp-25-1513-2025

Yu, Q., Jervis, D., & Huang, Y. (2024). Accounting for the effect of aerosols in GHGSat methane retrieval. *Atmos. Meas. Tech.*, 17, 3347–3366. https://doi.org/10.5194/amt-17-3347-2024

Zhu, X.-H., Lu, K.-F., Peng, Z.-R., He, H.-D., & Xu, S.-Q. (2022). Spatiotemporal variations of carbon dioxide (CO_2) at urban neighborhood scale: Characterization of distribution patterns and contributions of emission sources. *Sustain. Cities Soc.*, 78, 103646. https://doi.org/10.1016/j.scs.2021.103646